


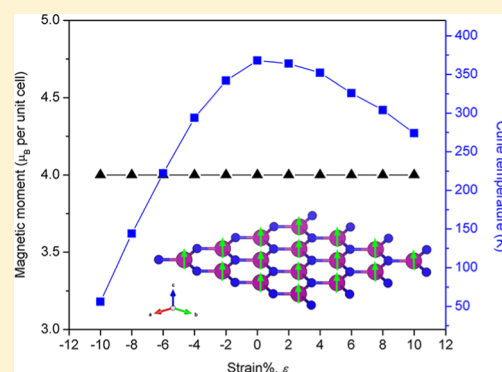
Two-Dimensional Manganese Nitride Monolayer with Room Temperature Rigid Ferromagnetism under Strain

Zhenming Xu and Hong Zhu*

University of Michigan–Shanghai Jiao Tong University Joint Institute, Shanghai Jiao Tong University, 800, Dongchuan Road, Shanghai 200240, China

Supporting Information

ABSTRACT: Developing low-dimensional spintronic materials with room temperature magnetic ordering and large spin polarization is the key for the fabrication of practical spintronic devices with a high circuit integration density and speed. Here, first-principles calculations were performed to systematically investigate a two-dimensional hexagonal MnN monolayer with room temperature magnetic ordering and 100% spin polarization. The MnN monolayer is thermally, dynamically, and mechanically stable, and intrinsically half-metallic with a very wide band gap. The Curie temperature of the MnN monolayer is estimated to be ~ 368 K, which is higher than room temperature and insensitive to strain. The MnN monolayer shows half-metallic and excellent magnetic stability upon the external strain from -10 to 10% . Our calculations indicate that the MnN monolayer could be a promising material for room temperature spintronic devices.



INTRODUCTION

Graphene, discovered by Andre Geim and co-workers by a simple method of scotch tape stripping in 2004, opens a new era of studying and applying two-dimensional (2D) materials.^{1–4} The reduction of material dimension gives rise to the novel physical and chemical properties, which are quite different from that of the three-dimensional (3D) structure.^{5,6} Two-dimensional materials can be widely applied in many fields, such as nanoelectronic and optical devices,^{7–10} energy storage,^{11–16} catalysis,^{17–20} and chemical sensors.^{21–23}

Nanoelectronic devices, especially for spintronics, which are urgently needed for developing high speed and low energy consuming information technology, are one of the most important application areas for 2D materials.²⁴ This is due to the fact that fabricating spintronic devices at nanoscale based on the low-dimensional spintronic materials can achieve high integration density and speed.²⁴ However, most 2D materials like graphene,^{1,3} graphdiyne,^{25,26} phosphorene,^{27,28} h-BN,^{29,30} borophene,³¹ etc. intrinsically show nonmagnetic or weakly magnetic characteristics, which limit their applications in spintronics. In general, a practical spintronic material should have a sizable room temperature magnetic moment, which means that a large spin polarization of an electron state around the Fermi energy level is essential.²⁴ Among many reported 2D materials, only a few 2D transition metal (TM) carbides, nitrides, sulfide, and trihalides show intrinsic ferromagnetism, such as Ti_2C ,³² Cr_2C ,³³ Mn_2C ,³⁴ FeC_2 ,³⁵ Ti_2N ,³² CrN ,³⁶ MoN_2 ,³⁷ MoS_2 ,^{38,39} NbS_2 ,⁴⁰ and TMX_2 transition metal dihalide ($X = \text{Cl}, \text{Br}, \text{and I}$) monolayers,^{41,42} in which the unpaired d-electrons in transition metals contribute to the formation of the spin-polarized electronic states. In addition,

earlier reports suggest that the incorporation of transition metal (TM) into metal-free 2D materials such as graphene^{43,44} and carbon nitride^{45,46} could induce a local magnetic moment and also lead to half-metallicity.

Here, we report a room temperature ferromagnetic (FM) and half-metallic 2D hexagonal manganese nitride with 100% spin polarization and high Curie temperature, which may be synthesized by a spontaneous graphitic conversion from the ultrathin (111)-oriented cubic MnN in the future experiments.⁴⁷ Similar spontaneous graphitizations of the ultrathin cubic structures can be found in diamond, boron nitride, and rock salt.⁴⁷ In this work, using first-principles calculations and ab-initio molecular dynamics (AIMD) simulations based on the density functional theory (DFT), we have systematically investigated the hexagonal MnN monolayer to ascertain its potential application for spintronic devices. Firstly, the thermal, dynamical, and mechanical stability of the MnN monolayer were confirmed by AIMD simulation, phonon dispersion calculation, and mechanical parameter calculation. Then, the spin-polarized electronic structures, magnetic properties, and Curie temperatures of the MnN monolayer with and without strain are discussed in detail.

COMPUTATIONAL METHODS

All atomic and electronic structure calculations were carried out by using the projector augmented wave method⁴⁸ in the framework of DFT,⁴⁹ as implemented in the Vienna ab-initio

Received: March 9, 2018

Revised: May 31, 2018

Published: June 6, 2018

simulation package. The generalized gradient approximation (GGA)⁵⁰ and Perdew–Burke–Ernzerhof exchange–correlation functional⁴⁹ are used. The electron configurations of Mn and N atoms are $3p^64s^23d^5$ and $2s^22p^3$, respectively. To consider the strong correlation effects of the transition metal Mn element, structural optimizations were performed by using the spin-dependent GGA plus Hubbard correction U (GGA + U) method.⁵¹ The Hubbard U parameter of Mn atom is set to 5.5 eV based on the previous study on the manganese(III) compound.⁵² For more accurate descriptions of electronic structures, the hybrid functional HSE06^{53,54} is employed for band structure and density of electron state (DOS) calculations. A vacuum region of 15 Å is applied to avoid interactions between the neighboring configurations. After convergence tests (see details in the Supporting Information, Table S1), the plane wave energy cutoff is set to 520 eV. The Monkhorst–Pack method⁵⁵ with $11 \times 11 \times 1$ and denser $25 \times 25 \times 1$ k -point meshes are employed for the Brillouin zone sampling, respectively, for structural relaxations and electronic structure calculations. The convergence criteria of energy and force calculations are set to 10^{-5} eV/atom and 0.01 eV Å⁻¹, respectively. The phonon calculations were performed with a $3 \times 3 \times 1$ supercell based on the density functional perturbation theory,⁵⁶ as implemented in the PHONOPY code.⁵⁷ In addition, ab-initio molecular dynamics (AIMD) simulations based on the Born–Oppenheimer approximation were performed at room temperature of 300 K in a statistical ensemble with a fixed particle number, volume, and temperature (NVT) by using a $3 \times 3 \times 1$ supercell of the MnN monolayer as the initial structure. The time step is set to 3 fs, and the supercell systems were simulated for 10 000 steps, with a total of 30 ps. A plane wave energy cutoff of 350 eV, Gamma-point for k -space mesh, and periodic boundary conditions were also used for AIMD simulations.

RESULTS AND DISCUSSION

Geometry and Stability. Our proposed graphene-like MnN monolayer belongs to the hexagonal honeycomb structure, and the corresponding atomic structure is depicted in Figure 1. The optimized lattice constant a of the MnN monolayer is 3.388 Å, and the corresponding Mn–N bond length is 1.956 Å. To confirm the dynamical stability of the MnN monolayer, its phonon dispersion was firstly calculated, as depicted in Figure 2a. All of the vibrational modes of our predicted MnN monolayer show positive frequencies, indicat-

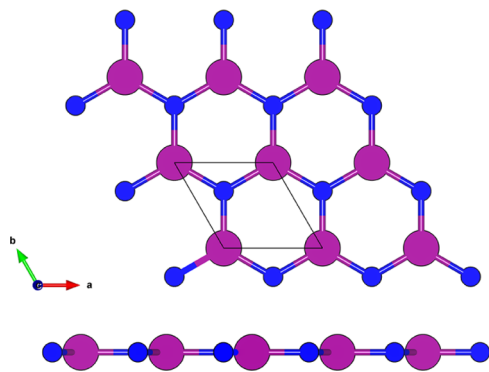


Figure 1. Schematic diagrams of the top and side views of the 2D MnN $2 \times 2 \times 1$ supercell structure, the purple and blue balls represent Mn and N atoms, respectively.

ing the MnN monolayer is stable or at least structurally metastable. The vibrational modes with lower frequencies (less than 450 cm⁻¹) are composed of three acoustic branches and one optical branch. Viewed from the total and partial density of phonon states, the Mn atom with a greater atomic mass mainly devotes to the acoustic vibrational modes with lower frequencies, whereas the high-frequency optical branches especially for those above 800 cm⁻¹ are mainly contributed by the N atom with a smaller atomic mass, separated from the lower frequency optical vibrational modes by a phonon gap of 350 cm⁻¹.

Then, AIMD simulations were performed by using a $3 \times 3 \times 1$ supercell of the MnN monolayer at 300 K for 30 ps to examine its thermal stability. During the whole AIMD simulation process, the total potential energies of the MnN monolayer vibrate around a constant of ~ 8.38 eV/atom, and the fluctuations of the total potential energy during the last 10 ps are ~ 20 meV/atom, as shown in Figure 2b. In addition, the supercell structure after 30 ps AIMD simulations nearly maintains the initial hexagonal honeycomb structure with some weak puckers, as illustrated in the inset of Figure 2b, which indicates the thermal stability of the MnN monolayer. The elastic constants of the MnN monolayer were also calculated to further verify its mechanical stability.^{58,59} According to the Born elastic theory,^{60,61} the elastic constant constitutes a symmetric 6×6 tensor matrix in the linear elastic range. Our calculated elastic constants are $C_{11} = 36.663$ GPa, $C_{22} = 36.663$ GPa, $C_{12} = 32.193$ GPa, and $C_{44} = 2.235$ GPa, respectively (see details in the Supporting Information, Table S2). All these elastic constants comply well with the Born criteria for 2D hexagonal crystal,^{60,61} that is, $C_{11} > 0$, $C_{22} > 0$, $C_{44} > 0$, and $C_{11}C_{22} - C_{12}^2 > 0$, confirming the MnN monolayer is mechanically stable. All above analyses of the dynamical, thermal, and mechanical properties of the MnN monolayer consistently demonstrate its stability in the ambient environment.

Electronic Structure and Magnetic Properties at Equilibrium Lattice. The electronic structures and magnetic properties of the material at an equilibrium lattice are important to investigate its potential application for spintronic devices. We firstly found that the total energy of the spin-polarized MnN monolayer is lower than that of the spin-unpolarized MnN monolayer by more than 0.40 eV/atom. Then, we calculated the magnetocrystalline anisotropy energies (MAEs) of the MnN unit cell by considering the effect of spin–orbit coupling. Herein, two magnetization directions in-plane, namely [100] and [110] directions, and two directions out-of-plane, namely [001] and [111] directions, are considered. The calculated MAEs by the HSE06 hybrid functional for the [100], [110], and [111] directions are 135.59, 134.27, and 160.00 μ eV/Mn atom relative to the [001] direction, respectively, as shown in Table S3, which indicates that the magnetic moment along the [001] direction (out-of-plane) is much more stable than other directions. Thus, the easy axis of the MnN monolayer is along the [001] direction (out-of-plane), which is consistent with 2D Fe₂Si⁶² and FeC₂³⁵ sheets.

The 4×4 supercells of the MnN monolayer with one ferromagnetic (FM) and six antiferromagnetic (AFM) spin orderings along the [001] direction were constructed based on the previous work of 2D hexagonal ferromagnetic materials,^{42,63} as schematically shown in Figure S1. The exchange energy (E_{ex}) between FM and AFM spin ordering structures is

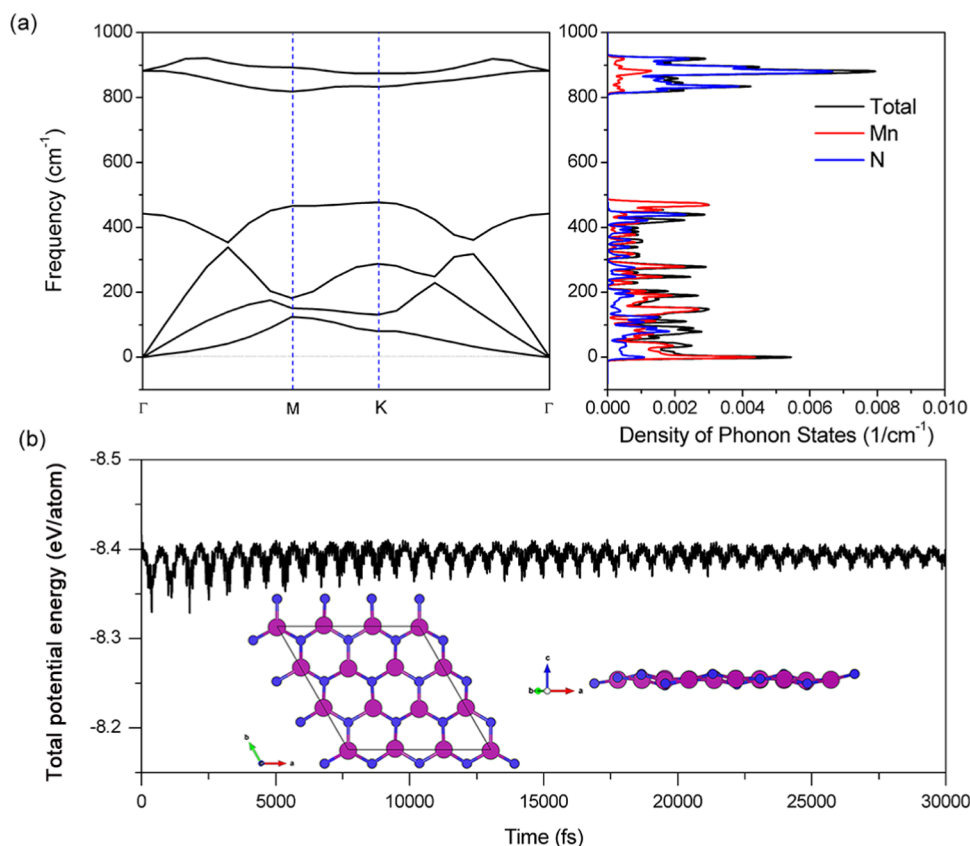


Figure 2. (a) Phonon spectrum, total and partial density of phonon states; (b) total potential energy fluctuations of the MnN monolayer during 30 ps AIMD simulation at 300 K, and the final puckered structures after AIMD simulation are also shown.

thus calculated by the formula $E_{\text{ex}} = E_{\text{AFM}} - E_{\text{FM}}$ based on the GGA + U method, which has been already successfully applied for 2D metal halides.⁴² If the exchange energy is positive, the ground state of the 2D MnN monolayer system is ferromagnetic. To evaluate the sensitiveness of the magnetic state to the Hubbard U parameter, E_{ex} of the MnN 4×4 supercells with different U values have been calculated, as shown in Figure S2. This confirms that the FM state is more preferable than the AFM state for all considered U values and E_{ex} converges to 0.410 eV/Mn atom around $U = 6.0$ eV, which validates our choice for the Hubbard U parameter for the manganese element of 5.5 eV based on the previous study on the manganese(III) compound.⁵² According to these calculated positive exchange energies of other antiferromagnetic (AFM) spin orderings (Figure S1), the MnN monolayer prefers the FM ground state with the magnetic moment along the [001] direction. Therefore, we only focus on the FM ground state with the magnetic moment along the [001] direction to study the electronic structures and magnetic properties in the following parts.

The spin-polarized band structures and total density of electron states (TDOS) were calculated at the HSE06 level for better understanding of the electronic structures and magnetic properties of the MnN monolayer. As shown in Figure 3, the MnN monolayer exhibits completely different electron conductivities of the spin-up and spin-down channels. The spin-down channel shows a very large direct band gap of 5.249 eV with an insulator feature, whereas the spin-up channel shows metallic characteristics due to the considerable occupied electron states cross the Fermi energy level. Therefore, the MnN monolayer is intrinsically half-metallic, and hence has

100% spin polarization near the Fermi level, which is quite different from its rock salt-structured phase without any spin polarization (Figure S3). Moreover, the partial density of electron states and partial charge distributions were also calculated to understand the bonding mechanism of Mn–N (see detailed discussion in Supporting Information, Figure S4).

We note from Figure S4 that the Mn $3d_z^2$ orbital is nondegenerate and does not bond to other orbitals. The double-degenerate Mn $3d_{xz}$ and $3d_{yz}$ spin-up and spin-down states overlap with N p_z states and form π -type bonding orbitals parallel to the plane of the MnN monolayer. The Mn $3d_{xy}$ and Mn $3d_{x^2-y^2}$ states are doubly degenerate, hybridizing with a Mn $4s$ state and forming three Mn sd^2 hybrid orbitals. These sd^2 hybrid orbitals overlap with three N sp^2 hybrid states and form a MnN hexagonal sheet. This Mn $3d$ orbital split is a typical picture for the trigonal-type complexes, which is quite different from the common $3d$ orbital splitting of the octahedral symmetry crystal with lower energy orbitals t_{2g} ($3d_{xy}$, $3d_{xz}$, and $3d_{yz}$) and higher energy orbitals e_g ($3d_{x^2-y^2}$ and $3d_z^2$).^{64,65} This is because of the fact that the symmetry and potential field of the Mn atom in this 2D MnN monolayer are different from that of the 3D octahedral crystal, which is consistent with the previous relevant report of the CrN monolayer.³⁶

Mn $4s$, $3d_{xy}$, and $3d_{x^2-y^2}$ orbitals strongly overlap with N $2s$, $2p_x$, and $2p_y$ orbitals, respectively, and two electrons from $3d_{xy}$ and $3d_{x^2-y^2}$ orbitals of the Mn atom exactly pair with two electrons from $2p_x$ and $2p_y$ orbitals of the N atom, respectively, leaving three unpaired $3d$ electrons of the Mn atom and one unpaired $2p$ electron of the N atom. Due to 100% spin polarization of these four unpaired valence electrons near the

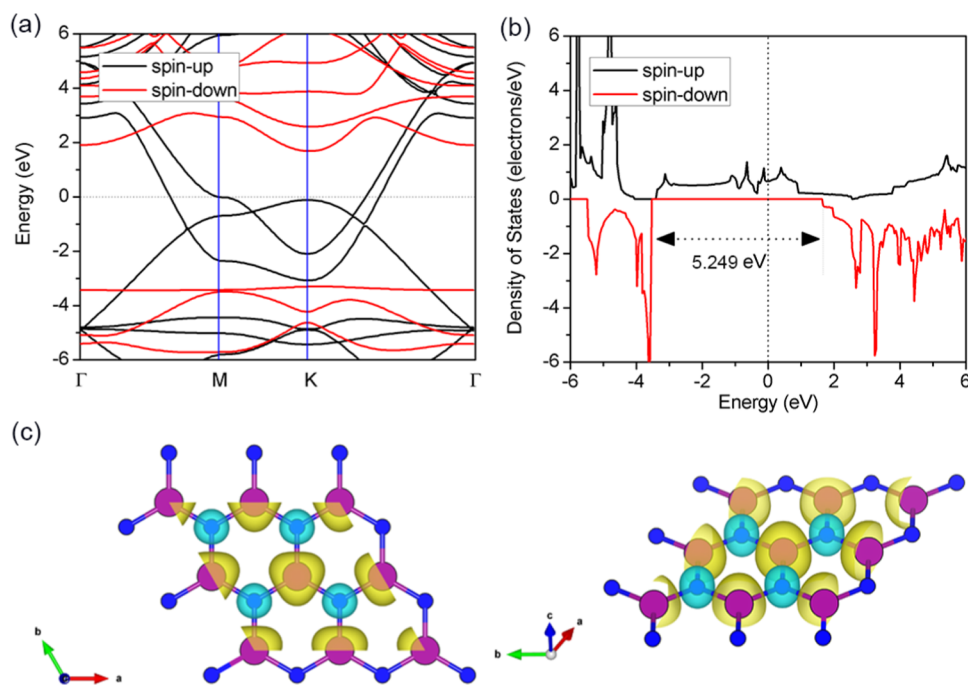


Figure 3. Electronic structure of the MnN monolayer at the HSE06 level. (a) Spin-polarized energy band structure of the MnN monolayer. (b) Spin-polarized total density of electron state (TDOS) of the MnN monolayer; spin-up and spin-down is depicted in black and red, respectively. The dashed lines in (a) and (b) indicate the Fermi level. (c) Top and side views of the spatial spin density distribution isosurfaces (0.01 e \AA^{-3}) of the MnN monolayer. The yellow and light-blue isosurfaces correspond to the spin-up and spin-down states, respectively.

Fermi level, the MnN monolayer has a net magnetic moment of $4 \mu_{\text{B}}$ per unit cell. Here, the Mn atom contributes to three quarters of magnetism with major spin densities, as the spin charge density plots shown in Figure 3c. The MnN monolayer with a wide half-metallic gap and large spin polarization can effectively serve in room temperature spintronic devices.

Curie Temperature. The Curie temperature of ferromagnetism–paramagnetism transition for ferromagnetic materials near or above 300 K is another critical determining factor for the practical room temperature spintronic devices. The Kosterlitz–Thouless transition is unlikely to occur in the MnN monolayer⁶⁷ because the magnetic moment of the MnN monolayer prefers the out-of-plane [001] direction (see details in the Supporting Information, Table S3), and the calculated MAEs by the HSE06 method are comparable to the reported 2D Ising-like ferromagnetic CrXTe_3 and Fe_2Si sheets.^{62,66} Thus, the Curie temperature of the MnN monolayer can be estimated by using the statistical Monte Carlo (MC) simulations based on the Ising model. This calculation method has been widely used to estimate the Curie temperature of 2D materials.^{35,68} In the 2D Ising model, the nearest neighboring spin interactions can be approximately equivalent to an exchange constant J , and the spin system energy is described by the classical Hamiltonian of the Ising model:

$$H = - \sum_{i,j} J_{ij} S_i^z S_j^z$$

where J_{ij} represents the magnetic exchange coupling constant between the two neighboring i and j spins, and S_i^z and S_j^z are spin parallel or antiparallel to the vacuum direction of the 2D model, respectively, for i and j sites. The exchange coupling constant J can be evaluated from the exchange energy between the FM and AFM spin arrangements in Figure S1 in Supporting Information. Here, we adapted the highest energy

AFM spin arrangement for the exchange coupling constant J calculations based on the previous work about the 2D hexagonal crystal structures.^{42,63,69}

$$J = \frac{2E_{\text{ex}}}{zS^2}$$

where E_{ex} is 0.408 eV per Mn atom (unit cell), z is the number of the nearest neighbors around one Mn atom ($z = 6$ for 2D hexagonal crystal structure), and S is the net magnetic moments of $4 \mu_{\text{B}}$ per unit cell of the MnN monolayer. Therefore, the corresponding estimated exchange coupling constant J is determined here to be 8.499 meV.

Then, MC simulations for 10^5 steps by using the Metropolis algorithm and a 2D hexagonal 80×80 grid points with periodic boundary conditions were performed to study the ferromagnetic systems. The calculated magnetization per unit cell (Mn atom) of the unstrained MnN monolayer as a function of different temperatures is depicted in Figure 4a. Below the ice point of 273.15 K, all spins in the MnN monolayer are aligned in parallel, providing a FM state. However, when temperature exceeding 400 K spins tend to be randomly aligned due to the stronger temperature perturbation, resulting in zero net magnetization (PM state). Our calculated Curie temperature of the FM–PM phase transition for the MnN monolayer is ~ 368 K, which is higher than room temperature. This indicates that the MnN monolayer meets the basic conditions of applying ferromagnetic materials for the practical room temperature spintronic devices. In addition, our calculated Curie temperature of the MnN monolayer is comparable with some other 2D ferromagnetic materials, such as metal halides MX_2 ($X = \text{Cl, Br}$ and I) (23–138 K),⁴² CrSnTe_3 (170 K),⁶⁶ and FeC_2 (245 K).³⁵

Strain Effect. The effect of strain on the electronic structure and magnetism of 2D materials is another important

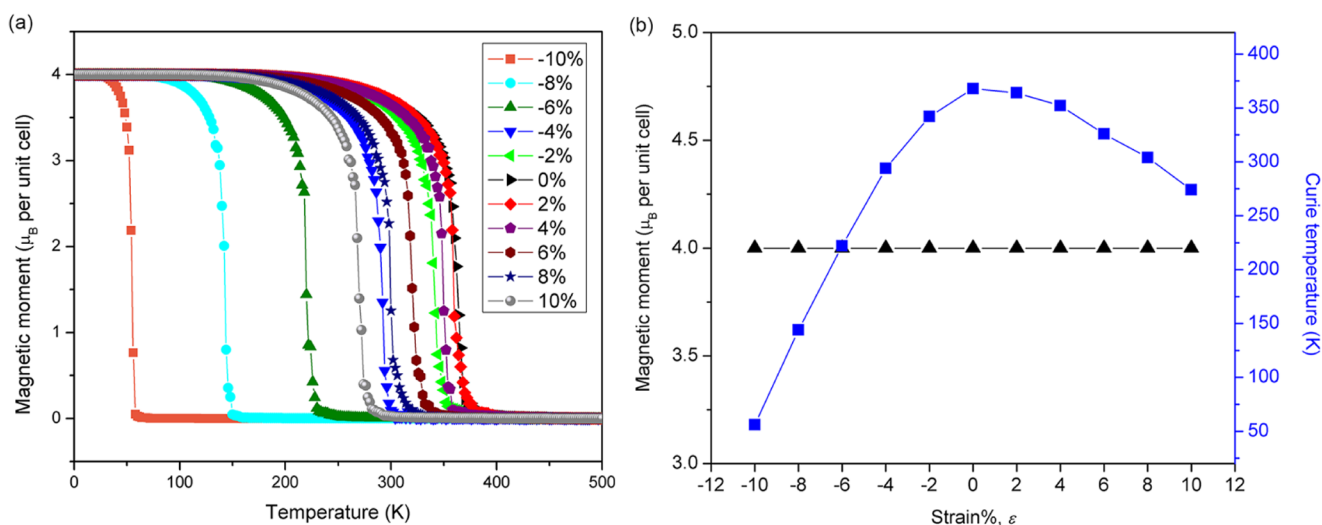


Figure 4. (a) Variations of the calculated magnetizations (in μ_B per unit cell) of the MnN monolayer with respect to different temperatures and equibiaxial strains. (b) Total magnetic moment (in μ_B per unit cell) at 0 K and Curie temperature of the MnN monolayer with respect to different equibiaxial strains.

concern for their applications in spintronic devices.^{37,40,70–72} Here, we studied the effect of strain on the electronic structures and magnetic properties of the MnN monolayer, and applied a series of equibiaxial strains from -10 to 30% to the MnN monolayer whose atomic positions were fully relaxed. The strain is defined as $\epsilon = (a - a_0)/a_0 \times 100\% = (b - b_0)/b_0 \times 100\%$, where a , b and a_0 , b_0 are the lattice constants of the unit cell under strain and at equilibrium, respectively. Here, the positive and negative ϵ represents the tensile and compressive strain, respectively. The lattice constant a , Mn–Mn, and the Mn–N bond length of the strained MnN monolayer systems are summarized in Table S4 in Supporting Information. The energy–strain and stress–strain curves of the MnN monolayer were calculated, as shown in Figure S5 in Supporting Information. Applying strains on the equilibrium monolayer can increase its total energy and stress, as expected. When applying equibiaxial strains from 20 to 30% , the stress of the MnN monolayer does not further change. We note that the equibiaxial strain of 30% does not exceed the elastic limit of the MnN monolayer, because no rapid attenuation of its stress response upon the application of strain is observed in Figure S5. Considering it is difficult to reach those strains more than 10% in the experimental operations and practical applications, we only focus on the variations of the electronic structure and magnetic properties of the MnN monolayer under different equibiaxial strains from -10 to 10% . The total magnetic moments (μ_B per unit cell) at the HSE06 level of the MnN monolayer with respect to the realistic equibiaxial strains from -10 to 10% were calculated, as shown in Figure 4b and summarized in Table S4 in Supporting Information. It can be seen that both these compressive and tensile strains do not change the total magnetic moment of the MnN monolayer at all.

For better understanding the rigidity of the total magnetic moment under different equibiaxial strains, the spin-polarized total density of electron states (TDOS) at the HSE06 level of the MnN monolayer under different equibiaxial strains from -10 to 10% were calculated, as depicted in Figure 5. The robust band gaps of the spin-down channels and the metal-like spin-up channels of these strained MnN monolayers are preserved, displaying 100% spin polarization near the Fermi

level, which are similar to the unstrained case. Band gaps and band edges of the spin-down electron state at the HSE06 level for the MnN monolayer under different strains are depicted in Figure 6. A closer look shows that the band gaps of the spin-down electron states decrease upon application of the compressive or tensile strains (Figure 6a), especially for the -8 and 10% strained systems, which are similar to those cases of the band gaps of 2D MoS₂^{73,74} and phosphorene (in the zigzag direction)⁷⁵ semiconductors decreasing under the tensile or compressive strains. It can be seen from Figure 6b that the valence band maximum (VBM) of the spin-down electron states with respect to the Fermi level goes up from -3.340 eV (unstrained system) to -2.891 eV (-6% compressive strain), and then goes down to -3.937 eV (-10% compressive strain) when the compressive strain increases from 0 to -10% . Meanwhile, the conduction band minimum (CBM) significantly shifts down from 1.909 to 0.625 eV when the compressive strain increases from 0 to -10% , whereas the shifts of the band edge do not display a linear function under strains. The nonlinear shifts of the energy-band-edge under strains can be explained by the Heitler–London’s exchange energy model⁷⁵ that the energy-band-edge shifts are closely related to the bonding/antibonding nature of the near-band-edge orbitals under strains.⁷⁶ Even when the MnN monolayer is under moderate strains (-2 and 2%), its VBM and CBM still shift significantly. During the stretching period with increased tensile strains from 0 to 10% , VBM markedly goes up from -3.340 to -2.415 eV, and CBM also shifts up from 1.909 to 2.194 eV (8% tensile strain), and then goes down to 2.177 eV (10% tensile strain). The increasing magnitude of VBM is larger than that of CBM, thus the corresponding band gaps of the spin-down states of those MnN monolayers under compressive strains significantly reduce. Moreover, we also calculated the DOS of these strained MnN monolayers by the GGA + U method for validating those calculated results by the HSE06 method, as shown in Figures 6 and S6 in Supporting Information. The calculated CBM edges of the spin-down states by the HSE06 method are in good accordance with those by the GGA + U method, whereas the VBM edges and band gaps calculated by the HSE06 method are larger than those by the GGA + U

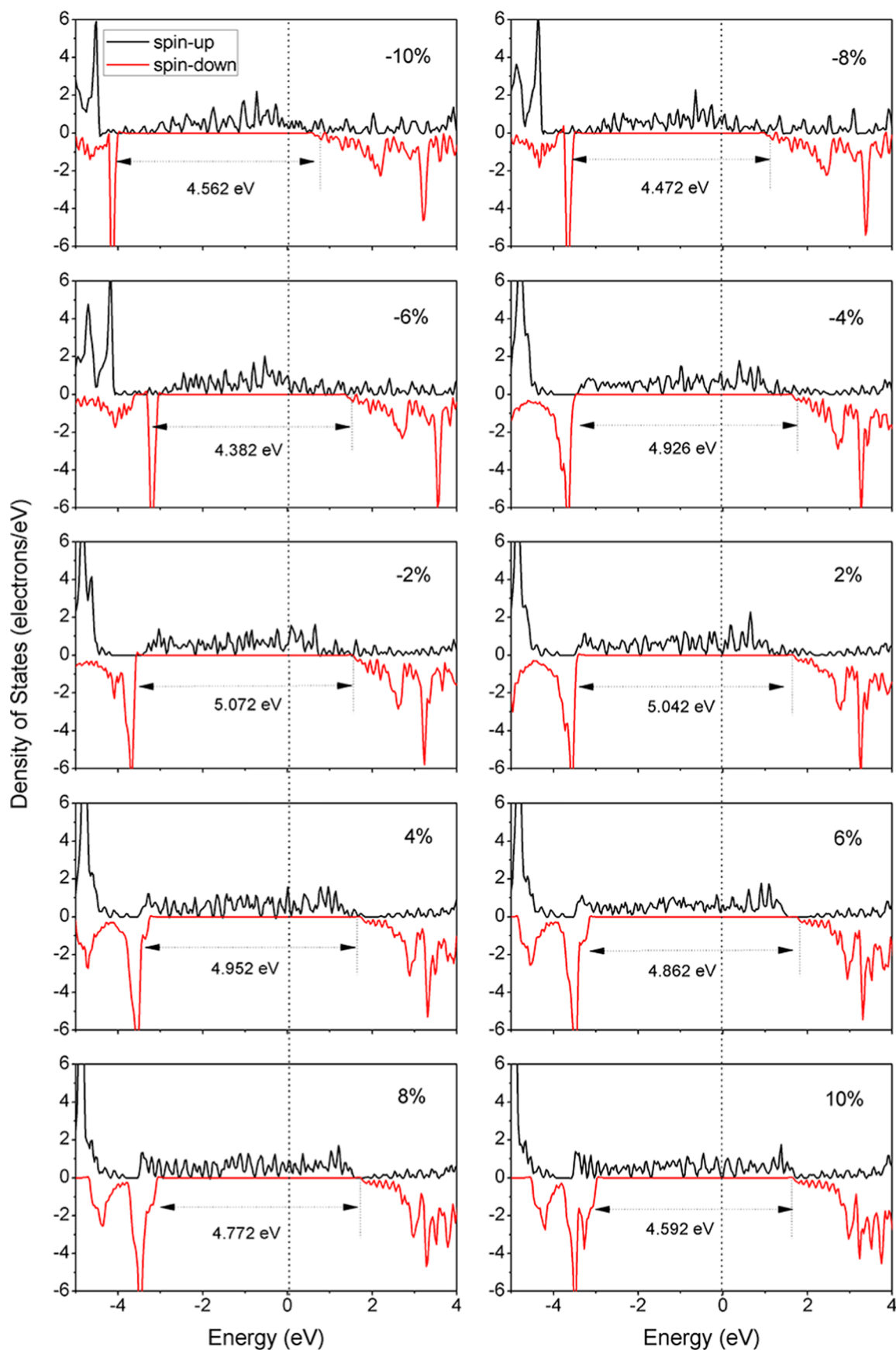


Figure 5. Spin-polarized total density of electron state (TDOS) near the Fermi level at the HSE06 level of the MnN monolayer under different equibiaxial strains. The dashed line means the Fermi level is set to 0 eV.

method, which is common for DFT calculation. Although there are absolute deviations between the band gaps calculated by these two methods, the variation trend of band gaps calculated by the HSE06 method is basically consistent with that by the GGA + U method. In this section, we only focus on the variations of the band gap under different strains rather than the absolute value, so both the HSE06 and GGA + U methods are competent for producing the variation in band gap.

In general, strains from -10 to 10% do not significantly change the electronic structure of the MnN monolayer (Figure 5), and 100% spin polarizations near the Fermi level of these strained systems are fully preserved by the robust band gaps of spin-down channels, so their magnetic properties are completely same as the unstrained system (Figure 4b). The MnN monolayer shows excellent FM half-metallic and magnetic stability under external strains from -10 to 10% , so the lattice mismatches between the MnN monolayer and substrate materials in the experimental synthetic process do not affect its magnetic property at all. This is different from the most reported two-dimensional materials with variational magnetic moments under strains,^{32,37,77} such as the half-metallic 2D Fe_2Si crystal with variable magnetic moments of $3.02\text{--}3.11 \mu_{\text{B}}$ under moderate strains (-3 to 3%).⁶² Our predicted MnN monolayer is promising to be used for the spin electronic devices where the stable spin magnetic moment against strain in the room environment is needed.

In addition, the dependence of Curie temperature of the MnN monolayer with respect to strain has also been studied. The energy difference between AFM and FM spin ordering structures under compressive strains sharply goes down from 0.325 to 0.057 eV per unit cell, and the tensile strained systems slightly go down to 0.275 eV per unit cell, as summarized in Table S4 in Supporting Information. It can be seen from Figure 4b that the response curve of Curie temperature vs strain is not monotonous, and it reduces more rapidly under enhanced compressive strains than those under enhanced tensile strains. In other words, Curie temperatures of these strained MnN monolayers decrease with the biaxial tensile or compressive strains, indicating that there is no room to ramp up the Curie temperature of the MnN monolayer by applying strain. Wu et al. showed that the tensile strain reduces the Curie temperature of the 2D Fe_2Si crystal, and the compressive strain enhances the Curie temperature, due to the monotonous variations of the Fe–Fe bond length resulting in the monotonous variations of the interaction between the neighboring Fe atoms,⁶² which is different from our MnN crystal with a nonmonotonous response. For 2D FeCl_2 , NbS_2 , and NbSe_2 crystals, their Curie temperatures can be dramatically enhanced by the tensile strains based on DFT calculations,^{42,69} in contrast to the 2D Fe_2Si crystal and our MnN monolayer. Experimentally, the enhancement of the Curie temperature by tensile stress has been carried out in the $\text{Fe}_{64}\text{Ni}_{36}$ Invar alloy because of the increase of the Fe–Fe interatomic distance.⁷⁸ Whereas for the single layer CrSnTe_3 , it is found that both compressive and tensile strains can reduce its Curie temperature,⁶⁶ which is consistent with our MnN monolayer. Therefore, the energy differences between the strained AFM and FM spin ordering structures (effective couple interactions between the neighboring magnetic atoms) are not the exclusive responses to structural deformations (bond length of neighboring magnetic atoms), and the variations of the electronic structure with respect to strains

may be another important factor. Interestingly, except for the cases of the strained MnN monolayers under larger compressive strains, the variation tendency of Curie temperature for the other strained MnN monolayers is generally in accordance with the variation curve of the band gap and the VBM edge of the spin-down electron state (Figure 6). As the protective effect of 100% spin polarization near the Fermi level gradually diminished by the reduced band gap under enhanced compressive or tensile strains, the energy differences between the FM and AFM structures get smaller, and FM spin ordering structures are more likely to switch to AFM or PM spin disordered structures. It is worth pointing out that some other important factors may also affect the Curie temperature of our strained MnN monolayer. More future efforts should be made to thoroughly figure out the general influence of structural deformation, electronic structure, and some other factors on the Curie temperature of 2D materials.

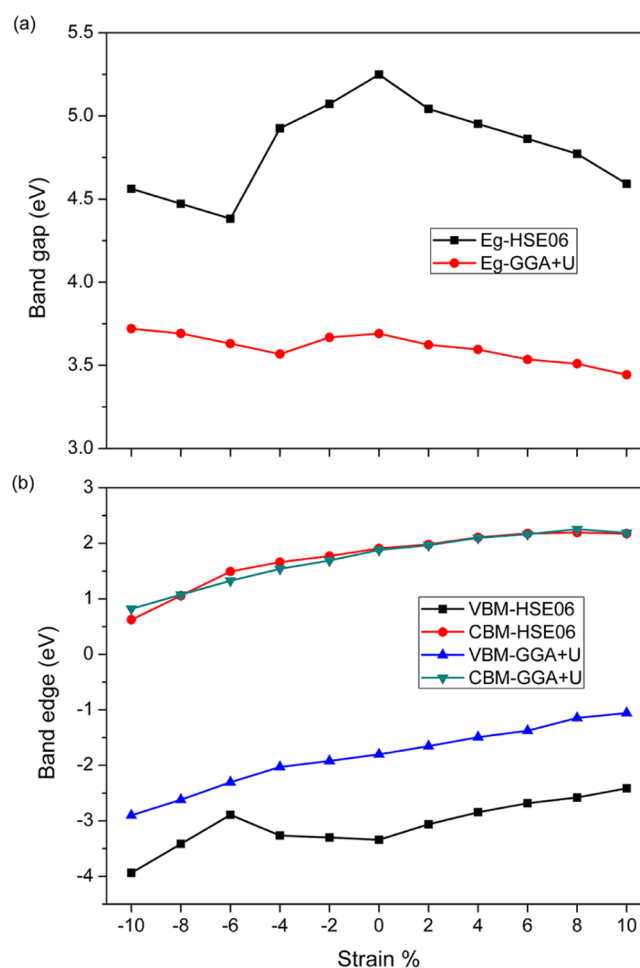


Figure 6. (a) Band gap (in eV) and (b) band edge (in eV) of the spin-down electron state of the MnN monolayer under different equal-biaxial strains. All energies are referenced to the vacuum level.

SUMMARY

A graphene-like two-dimensional hexagonal MnN monolayer with unique electronic structures and stable magnetic properties was studied by first-principles calculations. According to AIMD simulation, phonon spectra, and elastic constant analyses, the MnN monolayer is thermally, dynamically, and

mechanically stable. The electronic structure calculations indicate that the MnN monolayer is intrinsically half-metallic with a net magnetic moment of $4 \mu_B$ per unit cell, due to 100% spin polarization and the large band gap near the Fermi level. The Curie temperature of ~ 368 K of the MnN monolayer is estimated by MC simulations, which is higher than room temperature and not enhanced by strain. Different from most reported two-dimensional materials with variational magnetic moments under strain, the MnN monolayer can maintain the FM half-metallicity and a constant magnetic moment even under $\pm 10\%$ strain, due to 100% spin polarization electron states near the Fermi level being fully preserved by the robust band gap of the spin-down electron states. Our calculations indicate that the MnN monolayer could be a promising material for the room temperature spintronic devices.

■ ASSOCIATED CONTENT

Supporting Information

The Supporting Information is available free of charge on the ACS Publications website at DOI: [10.1021/acs.jpcc.8b02323](https://doi.org/10.1021/acs.jpcc.8b02323).

Energy cutoff and k -point convergence; elastic constants; magnetic anisotropy energies; lattice constant, magnetic moment, average energy difference between AFM and FM states, exchange coupling constant, energy band edge, and band gap of spin-down electron state with respect to different equibiaxial strains; AFM spin arrangements; energy difference between AFM and FM spin arrangements with different Hubbard correction U values; electronic structures of MnN rock salt-structured phase calculated by GGA; energies and stress response under different equibiaxial strains; spin-polarized TDOS at GGA + U level respect to different equibiaxial strains (PDF)

■ AUTHOR INFORMATION

Corresponding Author

*E-mail: hong.zhu@sjtu.edu.cn.

ORCID

Hong Zhu: [0000-0001-7919-5661](https://orcid.org/0000-0001-7919-5661)

Notes

The authors declare no competing financial interest.

■ ACKNOWLEDGMENTS

This work is supported by the National Natural Science Foundation of China (51602196) and the Shanghai Sailing Program (16YF1406000). All simulations were performed at the Shanghai Jiao Tong University High Performance Computing Center. The authors also thank Prof. Weidong Luo for the discussions.

■ REFERENCES

- (1) Loh, K. P.; Bao, Q.; Ang, P. K.; Yang, J. The chemistry of graphene. *J. Mater. Chem.* **2010**, *20*, 2277–2289.
- (2) Zhu, Y.; Murali, S.; Cai, W.; Li, X.; Suk, J. W.; Potts, J. R.; Ruoff, R. S. Graphene and graphene oxide: synthesis, properties, and applications. *Adv. Mater.* **2010**, *22*, 3906–3924.
- (3) Rao, C. N.; Sood, A. K.; Subrahmanyam, K. S.; Govindaraj, A. Graphene: the new two-dimensional nanomaterial. *Angew. Chem., Int. Ed. Engl.* **2009**, *48*, 7752–7777.
- (4) Novoselov, K. S.; Jiang, D.; Schedin, F.; Booth, T. J.; Khotkevich, V. V.; Morozov, S. V.; Geim, A. K. Two-dimensional atomic crystals. *Proc. Natl. Acad. Sci. U.S.A.* **2005**, *102*, 10451–10453.

- (5) Xu, M.; Liang, T.; Shi, M.; Chen, H. Graphene-like two-dimensional materials. *Chem. Rev.* **2013**, *113*, 3766–3798.

- (6) Zhang, H. Ultrathin Two-Dimensional Nanomaterials. *ACS Nano* **2015**, *9*, 9451–9469.

- (7) Lin, H.-F.; Liu, L.-M.; Zhao, J. 2D lateral heterostructures of monolayer and bilayer phosphorene. *J. Mater. Chem. C* **2017**, *5*, 2291–2300.

- (8) Novoselov, K. S.; Mishchenko, A.; Carvalho, A.; Castro Neto, A. H. 2D materials and van der Waals heterostructures. *Science* **2016**, *353*, No. aac9439.

- (9) Liu, Y.; Weiss, N. O.; Duan, X.; Cheng, H.-C.; Huang, Y.; Duan, X. Van der Waals heterostructures and devices. *Nat. Rev. Mater.* **2016**, *1*, No. 16042.

- (10) Xu, J.; Shim, J.; Park, J. H.; Lee, S. MXene Electrode for the Integration of WSe₂ and MoS₂ Field Effect Transistors. *Adv. Funct. Mater.* **2016**, *26*, 5328–5334.

- (11) Anasori, B.; Lukatskaya, M. R.; Gogotsi, Y. 2D metal carbides and nitrides (MXenes) for energy storage. *Nat. Rev. Mater.* **2017**, *2*, No. 16098.

- (12) Naguib, M.; Halim, J.; Lu, J.; Cook, K. M.; Hultman, L.; Gogotsi, Y.; Barsoum, M. W. New two-dimensional niobium and vanadium carbides as promising materials for Li-ion batteries. *J. Am. Chem. Soc.* **2013**, *135*, 15966–15969.

- (13) Liu, F.; Zhou, J.; Wang, S.; Wang, B.; Shen, C.; Wang, L.; Hu, Q.; Huang, Q.; Zhou, A. Preparation of High-Purity V₂C MXene and Electrochemical Properties as Li-Ion Batteries. *J. Electrochem. Soc.* **2017**, *164*, A709–A713.

- (14) Mashtalir, O.; Lukatskaya, M. R.; Zhao, M. Q.; Barsoum, M. W.; Gogotsi, Y. Amine-Assisted Delamination of Nb₂C MXene for Li-Ion Energy Storage Devices. *Adv. Mater.* **2015**, *27*, 3501–3506.

- (15) Liu, Y.; Zhao, Y.; Jiao, L.; Chen, J. A graphene-like MoS₂/graphene nanocomposite as a high-performance anode for lithium ion batteries. *J. Mater. Chem. A* **2014**, *2*, 13109–13115.

- (16) Xu, Z.; Lv, X.; Li, J.; Chen, J.; Liu, Q. A promising anode material for sodium-ion battery with high capacity and high diffusion ability: Graphyne and Graphdiyne. *RSC Adv.* **2016**, *6*, 25594–25600.

- (17) Rahman, M. Z.; Kwong, C. W.; Davey, K.; Qiao, S. Z. 2D phosphorene as a water splitting photocatalyst: fundamentals to applications. *Energy Environ. Sci.* **2016**, *9*, 709–728.

- (18) Deng, D.; Novoselov, K. S.; Fu, Q.; Zheng, N.; Tian, Z.; Bao, X. Catalysis with two-dimensional materials and their heterostructures. *Nat. Nanotechnol.* **2016**, *11*, 218–230.

- (19) Lukowski, M. A.; Daniel, A. S.; Meng, F.; Forticaux, A.; Li, L.; Jin, S. Enhanced hydrogen evolution catalysis from chemically exfoliated metallic MoS₂ nanosheets. *J. Am. Chem. Soc.* **2013**, *135*, 10274–10277.

- (20) Shi, X.-R.; Wang, S.; Hu, J.; Wang, H.; Chen, Y.-Y.; Qin, Z.; Wang, J. Density functional theory study on water–gas-shift reaction over molybdenum disulfide. *Appl. Catal., A* **2009**, *365*, 62–70.

- (21) González, C.; Biel, B.; Dappe, Y. J. Adsorption of small inorganic molecules on a defective MoS₂ monolayer. *Phys. Chem. Chem. Phys.* **2017**, *19*, 9485–9499.

- (22) Guo, H.; Zhang, W.; Lu, N.; Zhuo, Z.; Zeng, X. C.; Wu, X.; Yang, J. CO₂ Capture on h-BN Sheet with High Selectivity Controlled by External Electric Field. *J. Phys. Chem. C* **2015**, *119*, 6912–6917.

- (23) Hu, W.; Xia, N.; Wu, X.; Li, Z.; Yang, J. Silicene as a highly sensitive molecule sensor for NH₃, NO and NO₂. *Phys. Chem. Chem. Phys.* **2014**, *16*, 6957–6962.

- (24) Li, X.; Yang, J. First-principles design of spintronics materials. *Natl. Sci. Rev.* **2016**, *3*, 365–381.

- (25) Li, Y.; Xu, L.; Liu, H.; Li, Y. Graphdiyne and graphyne: from theoretical predictions to practical construction. *Chem. Soc. Rev.* **2014**, *43*, 2572–2586.

- (26) Ivanovskii, A. L. Graphynes and graphdienes. *Prog. Solid State Chem.* **2013**, *41*, 1–19.

- (27) Carvalho, A.; Wang, M.; Zhu, X.; Rodin, A. S.; Su, H.; Castro Neto, A. H. Phosphorene: from theory to applications. *Nat. Rev. Mater.* **2016**, *1*, No. 16061.

- (28) Ding, B.; Chen, W.; Tang, Z.; Zhang, J. Tuning Phosphorene Nanoribbon Electronic Structure through Edge Oxidization. *J. Phys. Chem. C* **2016**, *120*, 2149–2158.
- (29) Sun, Q.; Dai, Y.; Ma, Y.; Wei, W.; Huang, B. Lateral heterojunctions within monolayer h-BN/graphene: a first-principles study. *RSC Adv.* **2015**, *5*, 33037–33043.
- (30) Lin, Y.; Connell, J. W. Advances in 2D boron nitride nanostructures: nanosheets, nanoribbons, nanomeses, and hybrids with graphene. *Nanoscale* **2012**, *4*, 6908–6939.
- (31) Mannix, A. J.; Zhou, X.-F.; Kiraly, B.; Wood, J. D.; Alducin, D.; Myers, B. D.; Liu, X.; Fisher, B. L.; Santiago, U.; Guest, J. R.; et al. Synthesis of borophenes: Anisotropic, two-dimensional boron polymorphs. *Science* **2015**, *350*, 1513–1516.
- (32) Gao, G.; Ding, G.; Li, J.; Yao, K.; Wu, M.; Qian, M. Monolayer MXenes: promising half-metals and spin gapless semiconductors. *Nanoscale* **2016**, *8*, 8986–8994.
- (33) Si, C.; Zhou, J.; Sun, Z. Half-Metallic Ferromagnetism and Surface Functionalization-Induced Metal–Insulator Transition in Graphene-like Two-Dimensional Cr₂C Crystals. *ACS Appl. Mater. Interfaces* **2015**, *7*, 17510–17515.
- (34) He, J.; Lyu, P.; Nachtigall, P. New two-dimensional Mn-based MXenes with room-temperature ferromagnetism and half-metallicity. *J. Mater. Chem. C* **2016**, *4*, 11143–11149.
- (35) Zhao, T.; Zhou, J.; Wang, Q.; Kawazoe, Y.; Jena, P. Ferromagnetic and Half-Metallic FeC₂ Monolayer Containing C₂ Dimers. *ACS Appl. Mater. Interfaces* **2016**, *8*, 26207–26212.
- (36) Kuklin, A. V.; Kuzubov, A. A.; Kovaleva, E. A.; Mikhaleva, N. S.; Tomilin, F. N.; Lee, H.; Avramov, P. V. Two-dimensional hexagonal CrN with promising magnetic and optical properties: A theoretical prediction. *Nanoscale* **2017**, *9*, 621–630.
- (37) Wang, Y.; Wang, S.-S.; Lu, Y.; Jiang, J.; Yang, S. A. Strain-Induced Isostructural and Magnetic Phase Transitions in Monolayer MoN₂. *Nano Lett.* **2016**, *16*, 4576–4582.
- (38) Luxa, J.; Jankovsky, O.; Sedmidubsky, D.; Medlin, R.; Marysko, M.; Pumera, M.; Sofer, Z. Origin of exotic ferromagnetic behavior in exfoliated layered transition metal dichalcogenides MoS₂ and WS₂. *Nanoscale* **2016**, *8*, 1960–1967.
- (39) Zhang, X.; Bao, Z.; Ye, X.; Xu, W.; Wang, Q.; Liu, Y. Half-metallic properties of 3d transition metal atom-intercalated graphene@MS₂ (M = W, Mo) hybrid structures. *Nanoscale* **2017**, *9*, 11231–11238.
- (40) Xu, Y.; Liu, X.; Guo, W. Tensile strain induced switching of magnetic states in NbSe₂ and NbS₂ single layers. *Nanoscale* **2014**, *6*, 12929–12933.
- (41) He, J.; Ma, S.; Lyu, P.; Nachtigall, P. Unusual Dirac half-metallicity with intrinsic ferromagnetism in vanadium trihalide monolayers. *J. Mater. Chem. C* **2016**, *4*, 2518–2526.
- (42) Kulish, V. V.; Huang, W. Single-layer metal halides MX₂ (X = Cl, Br, I): stability and tunable magnetism from first principles and Monte Carlo simulations. *J. Mater. Chem. C* **2017**, *5*, 8734–8741.
- (43) Luan, H.-X.; Zhang, C.-W.; Li, S.-S.; Zhang, R.-W.; Wang, P.-J. First-principles study on ferromagnetism in W-doped graphene. *RSC Adv.* **2013**, *3*, 26261–26265.
- (44) Maassen, J.; Ji, W.; Guo, H. Graphene spintronics: the role of ferromagnetic electrodes. *Nano Lett.* **2011**, *11*, 151–155.
- (45) Choudhuri, I.; Kumar, S.; Mahata, A.; Rawat, K. S.; Pathak, B. Transition-metal embedded carbon nitride monolayers: high-temperature ferromagnetism and half-metallicity. *Nanoscale* **2016**, *8*, 14117–14126.
- (46) Ghosh, D.; Periyasamy, G.; Pandey, B.; Pati, S. K. Computational studies on magnetism and the optical properties of transition metal embedded graphitic carbon nitride sheets. *J. Mater. Chem. C* **2014**, *2*, 7943–7951.
- (47) Sorokin, P. B.; Kvashnin, A. G.; Zhu, Z.; Tománek, D. Spontaneous graphitization of ultrathin cubic structures: A computational study. *Nano Lett.* **2014**, *14*, 7126–7130.
- (48) Blöchl, P. E. Projector augmented-wave method. *Phys. Rev. B* **1994**, *50*, 17953–17979.
- (49) Kohn, W.; Sham, L. J. Self-Consistent Equations Including Exchange and Correlation Effects. *Phys. Rev.* **1965**, *140*, A1133–A1138.
- (50) Perdew, J. P.; Burke, K.; Ernzerhof, M. Generalized Gradient Approximation Made Simple. *Phys. Rev. Lett.* **1996**, *77*, 3865–3868.
- (51) Dudarev, S. L.; Botton, G. A.; Savrasov, S. Y.; Humphreys, C. J.; Sutton, A. P. Electron-energy-loss spectra and the structural stability of nickel oxide: An LSDA + U study. *Phys. Rev. B* **1998**, *57*, 1505–1509.
- (52) Seo, D.-H.; Gwon, H.; Kim, S.-W.; Kim, J.; Kang, K. Multicomponent Olivine Cathode for Lithium Rechargeable Batteries: A First-Principles Study. *Chem. Mater.* **2010**, *22*, 518–523.
- (53) Heyd, J.; Scuseria, G. E.; Ernzerhof, M. Hybrid functionals based on a screened Coulomb potential. *J. Chem. Phys.* **2003**, *118*, 8207–8215.
- (54) Henderson, T. M.; Paier, J.; Scuseria, G. E. Accurate treatment of solids with the HSE screened hybrid. *Phys. Status Solidi B* **2011**, *248*, 767–774.
- (55) Monkhorst, H. J.; Pack, J. D. Special points for Brillouin-zone integrations. *Phys. Rev. B* **1976**, *13*, 5188–5192.
- (56) Baroni, S.; de Gironcoli, S.; Dal Corso, A.; Giannozzi, P. Phonons and related crystal properties from density-functional perturbation theory. *Rev. Mod. Phys.* **2001**, *73*, 515–562.
- (57) Togo, A.; Tanaka, I. First principles phonon calculations in materials science. *Scr. Mater.* **2015**, *108*, 1–5.
- (58) Liu, C. S.; Zhu, H. H.; Ye, X. J.; Yan, X. H. Prediction of a new BeC monolayer with perfectly planar tetracoordinate carbons. *Nanoscale* **2017**, *9*, 5854–5858.
- (59) Teng, Z. W.; Liu, C. S.; Yan, X. H. A CO monolayer: first-principles design of a new direct band-gap semiconductor with excellent mechanical properties. *Nanoscale* **2017**, *9*, 5445–5450.
- (60) Born, M.; Huang, K. *Dynamic Theory of Crystal Lattice*; Clarendon: Oxford, 1954.
- (61) Wang, J.; Yip, S.; Phillpot, S. R.; Wolf, D. Crystal instabilities at finite strain. *Phys. Rev. Lett.* **1993**, *71*, 4182–4185.
- (62) Sun, Y.; Zhuo, Z.; Wu, X.; Yang, J. Room-Temperature Ferromagnetism in Two-Dimensional Fe₂Si Nanosheet with Enhanced Spin-Polarization Ratio. *Nano Lett.* **2017**, *17*, 2771–2777.
- (63) Zhang, C.-w.; Yan, S.-s. First-Principles Study of Ferromagnetism in Two-Dimensional Silicene with Hydrogenation. *J. Phys. Chem. C* **2012**, *116*, 4163–4166.
- (64) Srivastava, A. M.; Brik, M. G. Crystal field studies of the Mn⁴⁺ energy levels in the perovskite, LaAlO₃. *Opt. Mater.* **2013**, *35*, 1544–1548.
- (65) Brik, M. G.; Srivastava, A. M. Comparative crystal field analysis of energy level schemes and nephelauxetic effect for Cr⁴⁺, Cr³⁺, and Mn⁴⁺ ions in Y₂Sn₂O₇ pyrochlore. *Opt. Mater.* **2013**, *35*, 1251–1256.
- (66) Zhuang, H. L.; Xie, Y.; Kent, P. R. C.; Ganesh, P. Computational discovery of ferromagnetic semiconducting single-layer CrSnTe₃. *Phys. Rev. B* **2015**, *92*, No. 035407.
- (67) Carteaux, V.; Moussa, F.; Spiesser, M. 2D Ising-Like Ferromagnetic Behaviour for the Lamellar Cr₂Si₂Te₆ Compound: A Neutron Scattering Investigation. *Europhys. Lett.* **1995**, *29*, 251–256.
- (68) Kan, M.; Zhou, J.; Sun, Q.; Kawazoe, Y.; Jena, P. The Intrinsic Ferromagnetism in a MnO₂ Monolayer. *J. Phys. Chem. Lett.* **2013**, *4*, 3382–3386.
- (69) Zhou, Y.; Wang, Z.; Yang, P.; Zu, X.; Yang, L.; Sun, X.; Gao, F. Tensile strain switched ferromagnetism in layered NbS₂ and NbSe₂. *ACS Nano* **2012**, *6*, 9727–9736.
- (70) Liu, C.-S.; Teng, Z.-W.; Ye, X.-J.; Yan, X.-H. Two-dimensional tetragonal ALP monolayer: strain-tunable direct–indirect band-gap and semiconductor–metal transitions. *J. Mater. Chem. C* **2017**, *5*, 5999–6004.
- (71) Conley, H. J.; Wang, B.; Ziegler, J. I.; Haglund, R. F., Jr.; Pantelides, S. T.; Bolotin, K. I. Bandgap engineering of strained monolayer and bilayer MoS₂. *Nano Lett.* **2013**, *13*, 3626–3630.
- (72) Zhu, L.; Wang, S.-S.; Guan, S.; Liu, Y.; Zhang, T.; Chen, G.; Yang, S. A. Blue Phosphorene Oxide: Strain-tunable Quantum Phase

Transitions and Novel 2D Emergent Fermions. *Nano Lett.* **2016**, *16*, 6548–6554.

(73) He, K.; Poole, C.; Mak, K. F.; Shan, J. Experimental demonstration of continuous electronic structure tuning via strain in atomically thin MoS₂. *Nano Lett.* **2013**, *13*, 2931–2936.

(74) Scalise, E.; Houssa, M.; Pourtois, G.; Afanas'ev, V.; Stesmans, A. Strain-induced semiconductor to metal transition in the two-dimensional honeycomb structure of MoS₂. *Nano Res.* **2012**, *5*, 43–48.

(75) Peng, X.; Wei, Q.; Copple, A. Strain-engineered direct-indirect band gap transition and its mechanism in two-dimensional phosphorene. *Phys. Rev. B* **2014**, *90*, No. 085402.

(76) Peng, X.; Copple, A. Origination of the direct-indirect band gap transition in strained wurtzite and zinc-blende GaAs nanowires: A first principles study. *Phys. Rev. B* **2013**, *87*, No. 115308.

(77) Guo, H.; Lu, N.; Wang, L.; Wu, X.; Zeng, X. C. Tuning Electronic and Magnetic Properties of Early Transition-Metal Dichalcogenides via Tensile Strain. *J. Phys. Chem. C* **2014**, *118*, 7242–7249.

(78) Gorria, P.; Martínez-Blanco, D.; Pérez, M. J.; Blanco, J. A.; Hernando, A.; Laguna-Marco, M. A.; Haskel, D.; Souza-Neto, N.; Smith, R. I.; Marshall, W. G.; et al. Stress-induced large Curie temperature enhancement in Fe₆₄Ni₃₆ Invar alloy. *Phys. Rev. B* **2009**, *80*, No. 064421.